Parahydrogen-Polarized [1-13C]Pyruvate For Reliable and Fast Preclinical Metabolic Magnetic Resonance Imaging

Luca Nagel,‡[a] Martin Gierse,‡[b] Wolfgang Gottwald,‡[a] Zumrud Ahmadova,[b] Martin Grashei,[a] Pascal Wolff,[b] Felix Josten,[b] Senay Karaali,[b] Christoph A. Müller,[b] Sebastian Lucas,[b] Jochen Scheuer,[b] Christoph Müller,[b] John Blanchard,[b] Geoffrey J. Topping,[a] Andre Wendlinger,[a] Nadine Setzer,[a] Sandra Sühnel,[a] Jonas Handwerker,[b] Christophoros Vassiliou,[b] Frits H.A. van Heijster,[a] Stephan Knecht,[b]* Michael Keim,[b]* Franz Schilling,[a,c]*, Ilai Schwartz[b]*

[a] Department of Nuclear Medicine, TUM School of Medicine, Klinikum rechts der Isar of Technical University of Munich, 81675 Munich, Germany

[b] NVision Imaging Technologies GmbH, 89081 Ulm, Germany

[c] Munich Institute of Biomedical Engineering, Technical University of Munich, 85748 Garching, Germany

‡ shared first-authorship

* shared last-authorship

Abstract: Hyperpolarization techniques increase nuclear spin polarization by more than four orders of magnitude, enabling metabolic MRI. Even though the hyperpolarization has shown clear value in clinical studies, the complexity, cost and slowness of current equipment limits its widespread use. Here, we demonstrate a polarization procedure of [1-13C]pyruvate based on parahydrogen-induced polarization by side-arm hydrogenation (PHIP-SAH) in an automated polarizer. It was benchmarked in a study with 48 animals against a commercial dissolution dynamic nuclear polarization (DNP) device. We obtained purified, concentrated ($\approx$ 70-160 mM) and highly hyperpolarized ($\approx$ 18 %) solutions

of pyruvate at physiological pH for volumes up to 2 ml within 85 seconds in an automated process. The safety profile, image quality, as well as the quantitative perfusion and pyruvate-to-lactate ratios, were equivalent for PHIP and DNP, rendering PHIP a viable alternative to established hyperpolarization techniques.

Main Text: Since its introduction in 1973, magnetic resonance imaging (MRI) has provided non-invasive insights into living organisms with high soft-tissue contrast by means of low-energy radiofrequency fields[1]. Imaging physiological functions and microstructure continues to be a major motivation for driving innovation in the field and has resulted in a plethora of technologies and techniques that have reached clinical applications, including functional MRI (fMRI)[2], diffusion-weighted imaging (DWI)[3], and dynamic contrast-enhanced (DCE)-MRI[4]. A unique capability of magnetic resonance is the ability to assess molecular composition of tissue, using differences in the local magnetic fields experienced by nuclear spins, generating a difference in resonance frequency, also known as chemical shift. This enables liquid-state NMR spectroscopy techniques that are routinely used in various fields of chemistry, but have not yet been exploited for routine diagnostics in the clinic. This is partly due to the low sensitivity of NMR, resulting from the intrinsic small nuclear spin polarization at thermal equilibrium at clinically achievable field strengths, which prohibits molecular imaging at sufficient resolution. ^{1}H-MR spectroscopy suffers from long acquisition times and crowded spectra due to the relatively small spectral range, an abundance of different ^{1}H-nuclei and strong *J*-coupling. ^{13}C-MR spectroscopy on the other hand has a much larger spectral range and fewer different ^{13}C-nuclei, but the even lower sensitivity and only 1.1 % natural abundance of

NMR-visible carbon-13 render its use for molecular imaging applications extremely challenging. Conversely, positron emission tomography (PET) offers very high sensitivity, but involves patient exposure to potentially harmful ionizing radiation and cannot directly distinguish different molecules and their downstream metabolites labeled with the same radioactive isotope.

MR's sensitivity issue, in particular for carbon-13, can be addressed by hyperpolarization techniques[5]. An artificially high nuclear spin polarization, more than four orders of magnitude higher than at thermal equilibrium, is produced in exogenous agents, thereby boosting their measurable signal. In clinical studies, hyperpolarized noble gasses enabled visualization and quantification of lung ventilation[6] and hyperpolarized ^{13}C-labeled biomolecules facilitated the real-time measurement of metabolism in tumors, such as in the prostate[7] or in healthy and diseased brains[8].

Currently, the most widely used hyperpolarization technique is dissolution dynamic nuclear polarization (d-DNP), which requires a superconducting magnet and operates at liquid helium temperatures[9–11]. Although technically demanding, this technique allows a broad range of molecules to be polarized[12], is commercially available and is the standard technique for preclinical and clinical studies. There has been a focus on imaging the metabolism of hyperpolarized [1-^{13}C]pyruvate, as its downstream products allow quantification of both oxidative energy metabolism within the tricarboxylic acid cycle and of glycolytic lactate production[13]. Even though its clinical value for diagnosis and treatment response assessment has been demonstrated in several tumor entities, such as in the prostate[7], breast[14], and kidneys[15], the widespread use of hyperpolarized metabolic MRI is currently limited by the high cost and complexity of d-DNP instruments[11].

Novel technologies are needed to lower the hurdle for clinical translation and to allow more widespread use of hyperpolarized MRI. Two promising techniques exploit the highly polarized parahydrogen spin state, which is accessible at moderate temperatures using liquid nitrogen, to subsequently polarize [1-^{13}C]pyruvate, namely first via hydrogenation, termed "parahydrogen-induced polarization (PHIP)"[16,17], or second via reversible exchange with a binding complex, termed "signal amplification by reversible exchange (SABRE)"[18]. In cases for which direct hydrogenation is not feasible, such as for pyruvate and lactate, the introduction of the "parahydrogen-induced polarization by side-arm hydrogenation (PHIP-SAH)" approach has increased the applicability of that technique[19].

For PHIP-SAH induced hyperpolarization of pyruvate, the polarization process involves four key steps: 1) Derivatization of the carboxylate group with an unsaturated side-arm to form a pyruvate ester, 2) parahydrogenation of the unsaturated bond in the side-arm, 3) transfer of parahydrogen polarization to carbon nuclei and 4) hydrolysis for removal of the side-arm and catalyst.

Nevertheless, the use of hyperpolarized [1-^{13}C]pyruvate by PHIP-SAH and SABRE has been severely limited, compared to d-DNP, due to: (1) insufficient polarization and concentration for the required signal-to-noise ratio - so far, in vivo studies were reported with [1-^{13}C]pyruvate polarization levels at the time injection of ≈ 6-12 % for PHIP-SAH[19,20] and between 5-10 % for SABRE[21,22] with pyruvate concentration of ≈ 30-40 mM for both PHIP-SAH and SABRE; (2) a too high impurity profile, including rhodium or iridium from the catalyst and residual solvents that could induce toxicity (e.g. chloroform or methanol). Although the concentration of toxic catalyst solvents in the end product can be reduced - either by phase transfer[19], filtration[23] or precipitation and re-

dissolution[24] - it still represents a major challenge for the translation to the clinics.

Here, we show the culmination of several novel advances in the polarization of [1-^{13}C]pyruvate via PHIP-SAH, resulting in a fully-automated PHIP-SAH polarizer. Our prototype produces purified, concentrated (≈ 70-160 mM, depending on application) and highly hyperpolarized (≈ 18%) solutions of pyruvate at physiological pH and preclinically relevant volumes of up to 2 ml. We benchmark the prototype against a commercial d-DNP system in a preclinical study with 48 animals involving rats and mice, either healthy or tumor-bearing.

For the hyperpolarization of pyruvate via the PHIP-SAH process, we developed a pyruvate ester that is tailored for a rapid and highly selective hydrogenation reaction, while the side-arm system is hydrophobic. The use of a side-arm that has poor water solubility leads to a higher purity of the drug product, since the water phase can be effectively purified via extraction after cleavage. In previous studies, researchers predominantly chose organic solvents for the hydrogenation/polarization process that are poorly soluble in water, allowing a straightforward extraction process after the ester hydrolysis. However, we observed that the hydrogenation and especially the polarization of the ester works best in acetone, which is miscible with water. Therefore, we developed a fully automated process in six steps that enables the purification starting from an acetone mixture (Figure 1). Step 1: The ^{13}C labeled precursor (pyruvate ester with unsaturated C,C-triple bond in the side-arm) and the rhodium catalyst, dissolved in deuterated acetone, are injected into a reaction vessel (see methods section for experimental details). Step 2: The unsaturated triple-bond of the precursor is then hydrogenated with parahydrogen under elevated pressure and temperature. Step 3: The polarization transfer

takes place in a magnetic shield via radio-frequency sweeps [25]. Step 4: Subsequently, the solution is shuttled out of the magnetic shield into a vessel, where it is mixed with sodium hydroxide solution. The addition of the hydroxide initiates the cleavage of the hydrogenated pyruvate ester to sodium pyruvate and the hydrogenated side-arm. A buffered solution is added to adjust the pH value. Step 5: To initiate the phase separation of the organic and the aqueous phase, MTBE is added to the mixture. This separates the hydrophilic pyruvate in the aqueous phase from most of the acetone, the hydrogenated side-arm and catalyst in the organic phase. Thereafter, the aqueous phase is pumped into a vessel containing fresh MTBE as a further washing step, which reduces the organic impurities even further. Step 6: In the last process step, the aqueous phase is pumped to a heated vessel, in which nitrogen is bubbled through the solution at a reduced pressure. This reduces the MTBE and acetone concentration to around 6 mM and 90 mM, respectively. The whole purification process also reduces the rhodium concentration to under 10 µg/ml (see Table 1). During the whole purification process, the liquid stays inside a 100 mT permanent magnet. The extracted drug product (~ 2 mL) contains 160 mM sodium pyruvate with a polarization in the range of 18 %. To investigate lower concentrations, we prefilled the extraction syringe with D_2O and diluted the high pyruvate concentration coming from the polarizer. The entire process from sample injection to the extraction of the polarized, purified pyruvate takes 85 seconds.
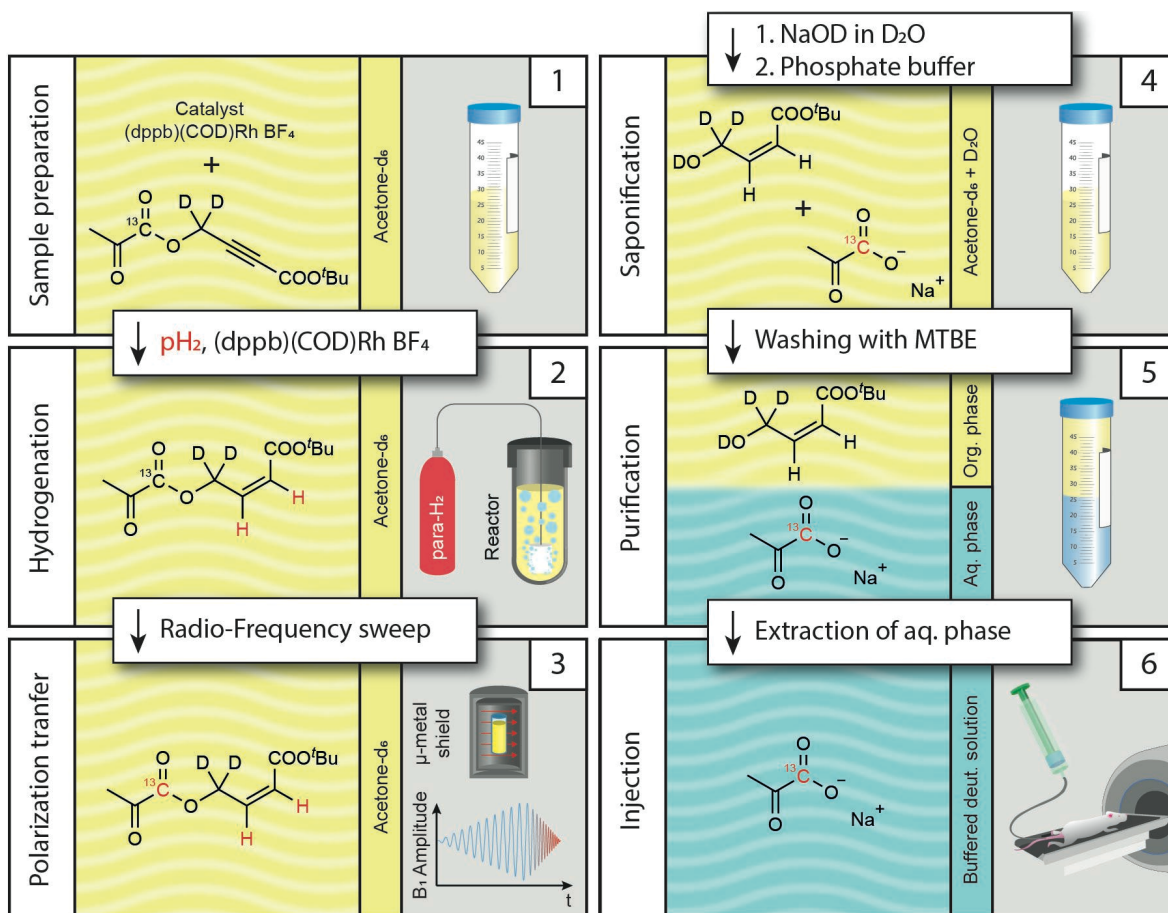
Figure 1. PHIP-SAH hyperpolarization of [1-^{13}C]pyruvate. First, the pyruvate ester is dissolved, together with the catalyst, in acetone-d$_6$. Second, the ester is hydrogenated with para-H$_2$ inside a reactor. Third, the polarization is transferred from the hydrogen to the ^{13}C nuclei via an rf-sweep in a magnetic shield. Fourth, the pyruvate is cleaved off and buffered. Fifth, MTBE is added to separate the pyruvate from the organic impurities. Sixth, the drug product is extracted and ready for injection. Note that all six steps are combined in one device (PHIP polarizer, see Supporting Figure S1).

Table 1. Impurity concentrations in the extracted pyruvate doses as measured after the automated hyperpolarization process (n = 5) .

Impurity	Concentration
Rhodium	7.16 ± 0.58 µg/ml
MTBE	5.7 ± 1.2 mM
Acetone	90 ± 16.6 mM

The above described process is performed within a fully automated single device.

In the following, this polarizer was compared to a standard dDNP polarizer (HyperSense, Oxford Instruments) with regard to the polarization level and differences in T_1 and T_2 for [1-^{13}C]pyruvate (Table 2).

We obtained slightly higher mean polarization values for DNP (22.8 %) vs. PHIP (17.8 %) at the time of injection. Pyruvate polarized with PHIP shows a significantly higher T_1 and shorter T_2 compared to DNP. Additionally, an increase in T_1 by using a deuterated solvent (114.0 s) vs. non deuterated solvent (58.4 s) was shown for DNP. The detailed measurement procedure and data analysis can be found in the methods part of the SI.

Table 2. Comparison of T_1, T_2 and polarization levels for DNP and PHIP protocols with standard deviations given.

	PHIP (D$_2$O)	DNP (D$_2$O)	DNP (H$_2$O)
Polarization level [%]	17.8 ± 1.3 (n=4)	22.8 ± 5.4 (n=7)	-
T_1 (1T) [s]	140.3 ± 6.0 (n=7)	114.0 ± 9.3 (n=6)	58.4 ± 4.0 (n=5)
T_1 (7T) [s]	105.3 ± 3.4 (n=3)	93.4 ± 8.6 (n=6)	56.7 ± 1.7 (n=5)
T_2 (7T) [s]	39.3 ± 1.8 (n=3)	56.7 ± 8.8 (n=6)	35.2 ± 4.1 (n=5)

To evaluate the perfusion properties of pyruvate for both methods 12 healthy animals (6 mice, 6 rats) received two intravenous pyruvate injections with a time interval between the two injections of 30 min (PHIP and DNP in mixed order). No significant difference between first and second injection was found (Supporting Information, Figure S4). Using a frequency-selective 3D balanced-steady state procession (bSSFP) sequence[26] pyruvate perfusion was monitored in abdominal organs and vessels over the time course of ≈ 100 s. Exemplary maximum intensity projections are shown in Fig. 2 for a rat (Fig. 2 a-f) and a mouse (Fig. 2 g-l) as well as the respective time courses for the same animal (Fig. 2 m). For PHIP and DNP images the calculated structural similarity index showed high similarity (SSIM = 0.95 ± 0.03 and SSIM = 0.88 ± 0.05 for rats and mice, respectively).
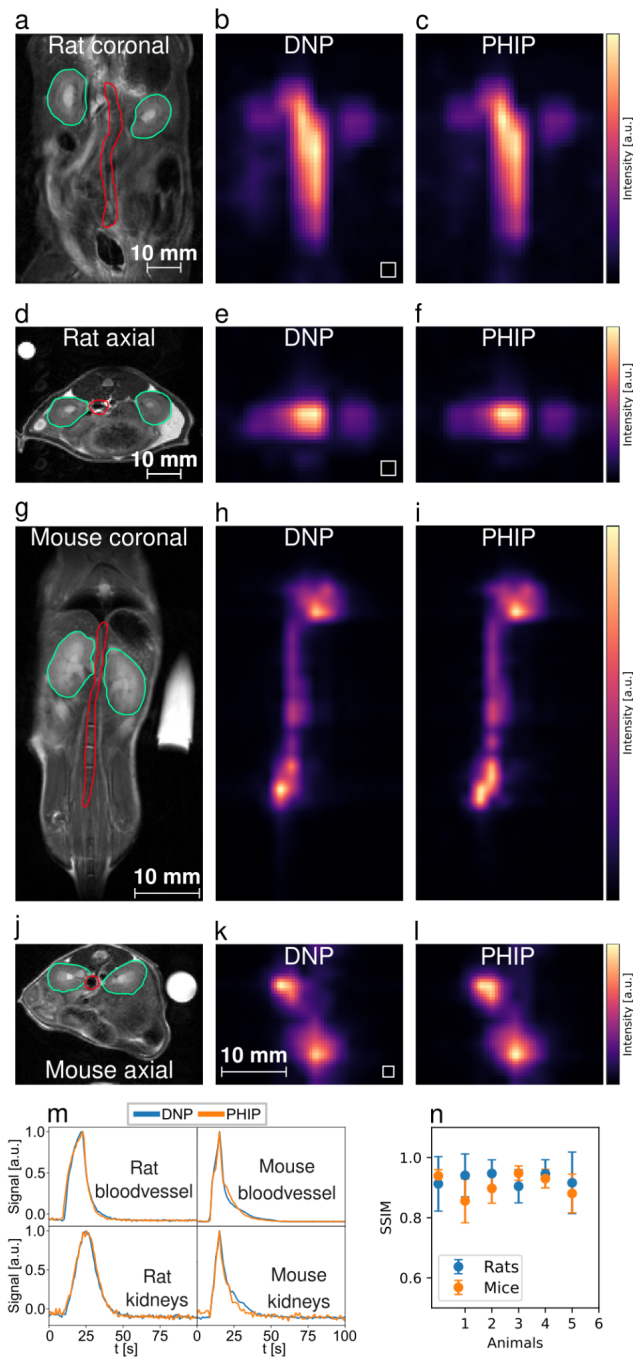
Figure 2. Comparison of perfusion between PHIP and DNP hyperpolarized [1-^{13}C]pyruvate using a single metabolite targeted spectrally-selective bSSFP sequence. (a-f), exemplary datasets from a healthy rat where (a) and (d) are the anatomical reference images with the segmented regions, namely the kidneys (green) and a central blood vessel (red), (b) and (c) show interpolated bSSFP maximum intensity

projections (MIPs) in coronal orientation with the original resolution shown as white boxes on the lower left, (e) and (f) shows MIPs in axial orientation. (g-l), pyruvate perfusion MIPs and their anatomical references from a healthy mouse. Visible are a central bloodvessel and the heart. The signal intensities (b, c, e, f, h, i, m, k, l) were scaled to maximum value for better comparability. (m), signal intensity time curves from blood vessels (red ROIs) and kidneys (green ROIs), (n), structural similarity indices (SSIM) showing a similar SSIM for rat (0.95 ± 0.03) and mouse (0.88 ± 0.05) measurements.
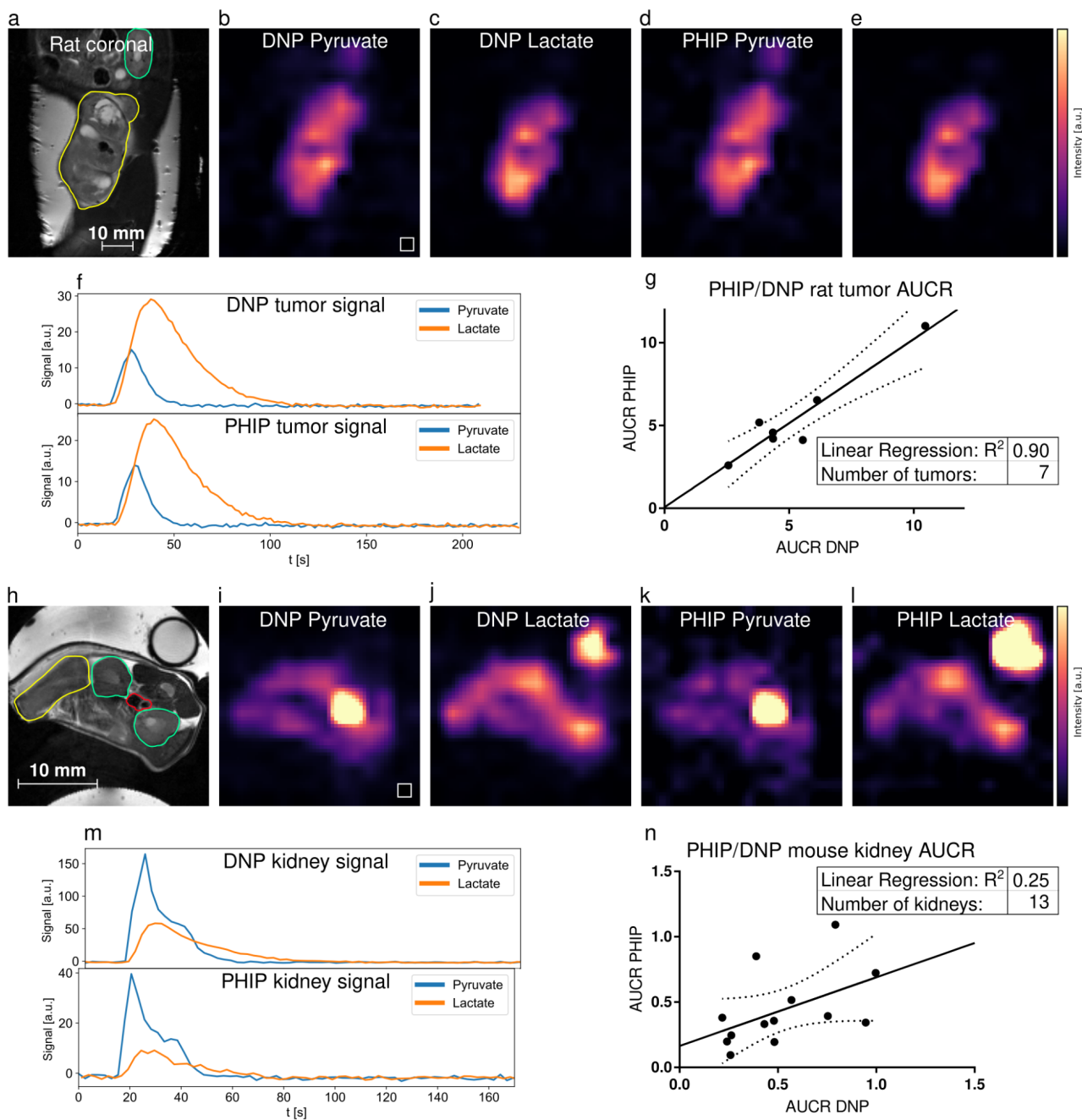
Figure 3. Comparison of metabolism in rat tumors and mice kidneys between PHIP and DNP hyperpolarized [1-^{13}C]pyruvate using a dual metabolite targeted spectrally-selective bSSFP sequence. (a-f), exemplary PHIP and DNP datasets of a Mat B III tumor-bearing rat. In the corresponding anatomical reference (a), the tumor and kidney are drawn in yellow and green, respectively. The tumor 3D ROI time curves of pyruvate and lactate are shown in (f). The signal intensities (b, c, d, e, i, j,

k, l) were scaled to maximum value for better comparability. (g), comparison of rat tumor lactate-to-pyruvate area-under-the-curve ratio (AUCR) of PHIP and DNP showing very good correlation between the two methods (R^2 = 0.90). (h-l), pyruvate and lactate distributions in a tumor-bearing mouse are shown, with the corresponding anatomical reference in (h). Tumor (yellow), kidneys (green) and the bloodvessel (red) ROIs are depicted. (m), signal intensity time curves from left kidney (green ROI). (n), correlation of PHIP and DNP AUCRs of mouse kidneys (R^2 = 0.27). Dashed lines in (g, n) indicate the 95 % confidence interval.

To evaluate the metabolic conversion of pyruvate to lactate, 8 tumor-bearing rats (Mat B III mammary adenocarcinoma) and 8 mice (EL4 lymphoma) received two intravenous pyruvate injections each with a time interval of 30 min between the two injections (PHIP and DNP in mixed order). Using a frequency-selective 3D balanced-steady state procession (bSSFP) sequence[26] alternating between pyruvate and lactate excitation, metabolism was monitored in the tumors and abdominal organs. Mean pyruvate and lactate distributions in one coronal slice for both PHIP and DNP are shown exemplary for a rat tumor (Figure 3, a-e) and a mouse kidney (Figure 3, h-l), together with their respective metabolite time curves (Figure 3, f, m). The calculated correlations of the area-under-the-curve ratios (AUCRs)[27] between PHIP and DNP were found to be high for rat tumors (R^2 = 0.90) and mouse tumors (R^2 = 0.98, see Supporting Information Figure S2) and low for mouse kidneys (R^2 = 0.27) and rat kidneys (R^2 = 0.52, see Supporting Information Figure S2).

Time-resolved slice-selective spectroscopy was performed for both PHIP and DNP in a Mat B III tumor-bearing rat (Figure 4, a, d, e, g) leading to almost qualitatively identical time curves and AUCRs. Furthermore, due

to the short operation time of the PHIP polarizer, 4 injections were given to 2 rats (one healthy, one tumor-bearing) with shortened time intervals of 15 minutes between injections, successfully demonstrating a high reproducibility of the experiments and high experimental throughput (Figure 4, b, c, f, h, i).
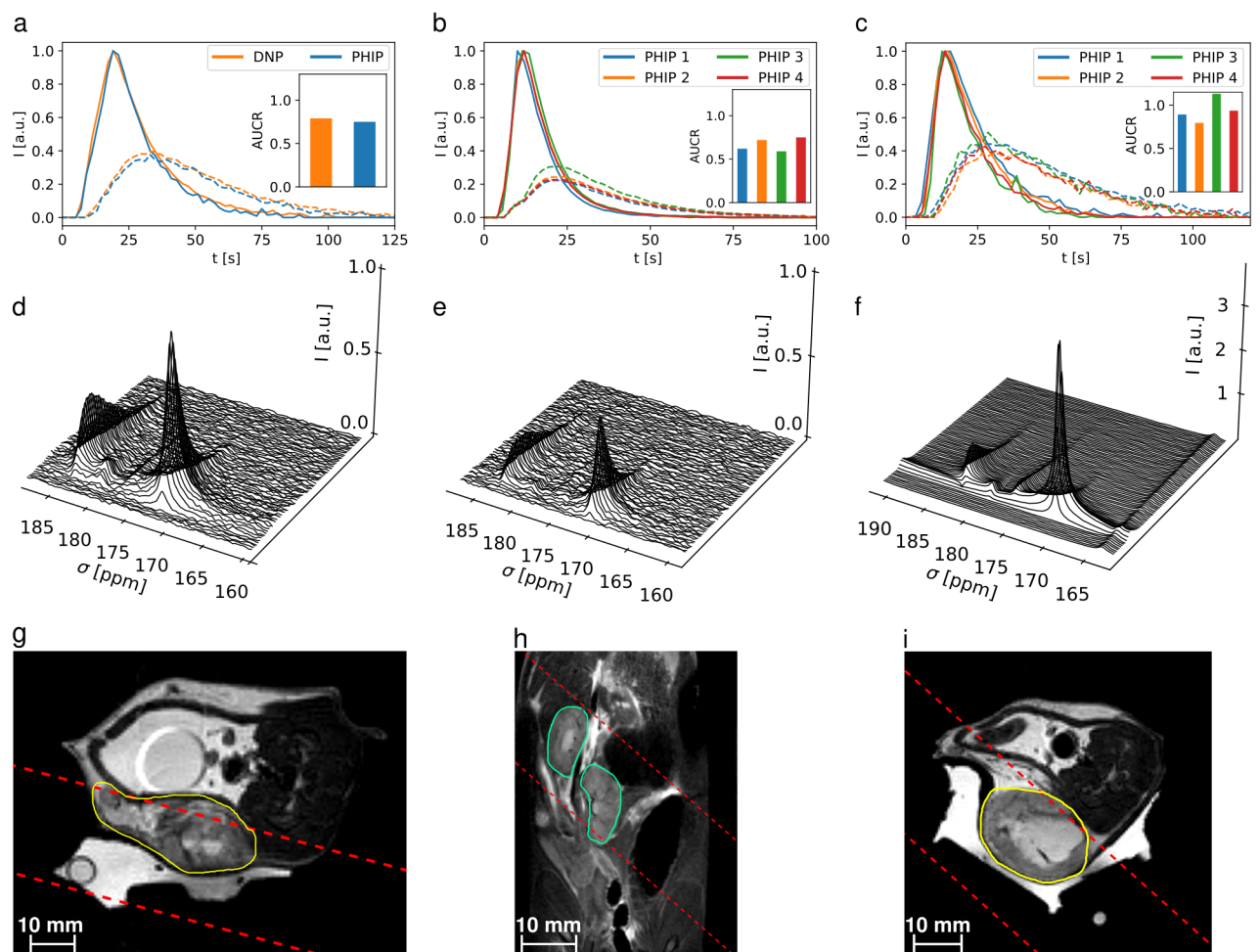

Figure 4. Comparison of slice-selective spectroscopy between PHIP and DNP as well as fast, repeated injections for PHIP. (a), time curves for DNP and PHIP injections in a subcutaneous MAT B III rat tumor model, with area under the curve ratio (AUCR) values in the insert. (b), time curves for

four repeated PHIP injections in a healthy rat. (c), shows time curves for four repeated PHIP injections in a subcutaneous MAT B III rat tumor model. AUC ratios from (b) and (c) are displayed in (f) for four PHIP injections, which show higher AUC in the tumor compared to a healthy kidney. (d, e) spectra from the DNP and PHIP injections in (a). (f), spectra from the second PHIP injection in (b). (g, h, i), slice placement for each experiment (a, b, c) in red and tumor (yellow) and kidneys (green) highlighted. Time curves were normalized and shifted to align their respective pyruvate peaks to facilitate direct comparison of peak shapes. Spectra shown in (d) and (e) had 15 Hz line broadening applied and are normalized to the largest pyruvate peak in the DNP spectrum (d), showing a higher signal for the DNP injection in (d), which can be explained due to a lower polarization level for the PHIP polarizer configuration.

For all animal experiments, rectal temperature, breathing rate and oxygen saturation were logged (Supporting Information, Figure S3). However, no substantial difference between the reaction to the PHIP or DNP injections on those vital parameters was found. Furthermore, there was no substantial deviation from what would be expected as a reaction due to any arbitrary intravenous injection. Also, there was no significant difference ($p > 0.05$) in AUCRs between first and second injections (Supporting Information, Fig. S4).

The achievement of reproducible $\approx$ 18 % polarization of purified [1-^{13}C]pyruvate at the time of injection into the animal required several key advancements in the PHIP-SAH process. First, the precursor ester was specifically designed for more efficient hydrogenation (full hydrogenation within 5 seconds) and high hydrophobicity of the side-arm residue following hydrolysis, leading to efficient washing of the residue with MTBE.

In addition, the full deuteration of the CH$_2$ group led to an enhancement of the singlet state order on the parahydrogenated protons. A challenge which had to be overcome was the lack of intermediate protons in the polarization transfer to the ^{13}C spin[25]. Careful characterization of the *J*-coupling network showed a direct coupling of 0.4 Hz between the parahydrogenated proton and the carbon spin, sufficient for direct transfer, leading to > 36 % ^{13}C spin polarization. Second, the entire purification process had to be optimized and fully automated to preserve as much of the polarization as possible while reducing all impurities to acceptable levels (Table 1). The development of precursor esters of other carboxylate probes for hyperpolarized ^{13}C-MRI utilizing the same side-arm form seems feasible.

In order to verify the reliability of our method, a rigorous in vivo analysis with 48 mice and rats was conducted. These experiments demonstrated that the described PHIP polarization and purification process is safe and reliable and provides the necessary signal-to-noise ratio for 3D metabolic imaging to obtain quantitative AUCR. In particular, we demonstrate for the hyperpolarized pyruvate solutions, independent whether produced by the PHIP or DNP method, similar perfusion in healthy animals' abdominal organs and similar pyruvate-lactate conversion. Following these results, PHIP-based hyperpolarization seems now all set to become a widespread method for hyperpolarized MRI. The short duration of the automated PHIP process allows for new kinds of experiments, such as leveraging rapid multi-dose experiments to obtain new metabolic insights or access to previously unfeasible experimental designs due to long polarization durations.

In conclusion, our study demonstrates that, for the first time, PHIP-based hyperpolarization of pyruvate can achieve comparable results with d-DNP regarding polarization, volume and concentration levels at the time of injection, yielding quantitatively similar perfusion and metabolic information in the in vivo experiments. The polarization time for [1-^{13}C]pyruvate ($\approx$ 85 seconds) for the PHIP prototype is much shorter than that ($\approx$ 45 minutes) for the d-DNP system.

Acknowledgements

Conflicts of Interest

The authors declare the following competing financial interests: MG, ZA, PW, FJ, SK, CAM, SL, JS, CM, JB, JH, CV, SK, MK, IS are or were employed by NVision Imaging Technologies GmbH. FS serves on the scientific advisory board of NVision Imaging Technologies GmbH.

Institute and/or researcher Twitter usernames: @schillinglab, @NVisionQuantum

References

[1] P. C. Lauterbur, Nature 1973, 242, 190–191.

[2] S. Ogawa, D. W. Tank, R. Menon, J. M. Ellermann, S. G. Kim, H. Merkle, K. Ugurbil, Proc. Natl. Acad. Sci. 1992, 89, 5951–5955.

[3] K.-D. Merboldt, W. Hanicke, J. Frahm, J. Magn. Reson. 1969 1985, 64, 479–486.

[4] S. H. Heywang, D. Hahn, H. Schmidt, I. Krischke, W. Eiermann, R. Bassermann, J. Lissner, J. Comput. Assist. Tomogr. 1986, 10, 199–204.

[5] J. Eills, D. Budker, S. Cavagnero, E. Y. Chekmenev, S. J. Elliott, S. Jannin, A. Lesage, J. Matysik, T. Meersmann, T. Prisner, J. A. Reimer, H. Yang, I. V. Koptyug, Chem. Rev. 2023, 123, 1417–1551.

[6] J. P. Mugler, T. A. Altes, I. C. Ruset, I. M. Dregely, J. F. Mata, G. W. Miller, S. Ketel, J. Ketel, F. W. Hersman, K. Ruppert, Proc. Natl. Acad. Sci. 2010, 107, 21707–21712.

[7] S. J. Nelson, J. Kurhanewicz, D. B. Vigneron, P. E. Z. Larson, A. L. Harzstark, M. Ferrone, M. van Criekinge, J. W. Chang, R. Bok, I. Park, G. Reed, L. Carvajal, E. J. Small, P. Munster, V. K. Weinberg, J. H. Ardenkjaer-Larsen, A. P. Chen, R. E. Hurd, L.-I. Odegardstuen, F. J. Robb, J. Tropp, J. A. Murray, Sci. Transl. Med. 2013, 5, DOI 10.1126/scitranslmed.3006070.

[8] J. T. Grist, M. A. McLean, F. Riemer, R. F. Schulte, S. S. Deen, F. Zaccagna, R. Woitek, C. J. Daniels, J. D. Kaggie, T. Matys, I. Patterson, R. Slough, A. B. Gill, A. Chhabra, R. Eichenberger, M.-C. Laurent, A. Comment, J. H. Gillard, A. J. Coles, D. J. Tyler, I. Wilkinson, B. Basu, D. J. Lomas, M. J. Graves, K. M. Brindle, F. A. Gallagher, NeuroImage 2019, 189, 171–179.

[9] J. H. Ardenkjær-Larsen, B. Fridlund, A. Gram, G. Hansson, L. Hansson, M. H. Lerche, R. Servin, M. Thaning, K. Golman, Proc. Natl. Acad. Sci. 2003, 100, 10158–10163.

[10] J. H. Ardenkjaer-Larsen, J. Magn. Reson. 2016, 264, 3–12.

[11] J. H. Ardenkjær-Larsen, S. Bowen, J. R. Petersen, O. Rybalko, M. S. Vinding, M. Ullisch, N. Chr. Nielsen, Magn. Reson. Med. 2019, 81, 2184–2194.

[12] K. R. Keshari, D. M. Wilson, Chem Soc Rev 2014, 43, 1627–1659.

[13] Z. J. Wang, M. A. Ohliger, P. E. Z. Larson, J. W. Gordon, R. A. Bok, J. Slater, J. E. Villanueva-Meyer, C. P. Hess, J. Kurhanewicz, D. B. Vigneron, Radiology 2019, 291, 273–284.

[14] F. A. Gallagher, R. Woitek, M. A. McLean, A. B. Gill, R. Manzano Garcia, E. Provenzano, F. Riemer, J. Kaggie, A. Chhabra, S. Ursprung, J. T. Grist, C. J. Daniels, F. Zaccagna, M.-C. Laurent, M. Locke, S. Hilborne, A. Frary, T. Torheim, C. Boursnell, A. Schiller, I. Patterson, R. Slough, B. Carmo, J. Kane, H. Biggs, E. Harrison, S. S. Deen, A. Patterson, T. Lanz, Z. Kingsbury, M. Ross, B. Basu, R. Baird, D. J. Lomas, E. Sala, J. Wason, O. M. Rueda, S.-F. Chin, I. B. Wilkinson, M. J. Graves, J. E. Abraham, F. J. Gilbert, C. Caldas, K. M. Brindle, Proc. Natl. Acad. Sci. 2020, 117, 2092–2098.

[15] S. Ursprung, R. Woitek, M. A. McLean, A. N. Priest, M. Crispin-Ortuzar, C. R. Brodie, A. B. Gill, M. Gehrung, L. Beer, A. C. P. Riddick, J. Field-Rayner, J. T. Grist, S. S. Deen, F. Riemer, J. D. Kaggie, F. Zaccagna, J. A. G. Duarte, M. J. Locke, A. Frary, T. F. Aho, J. N. Armitage, R. Casey, I. A. Mendichovszky, S. J. Welsh, T. Barrett, M. J. Graves, T. Eisen, T. J. Mitchell, A. Y. Warren, K. M. Brindle, E. Sala, G. D. Stewart, F. A. Gallagher, Cancers 2022, 14, 335.

[16] C. R. Bowers, D. P. Weitekamp, J. Am. Chem. Soc. 1987, 109, 5541–5542.

[17] J. Hövener, A. N. Pravdivtsev, B. Kidd, C. R. Bowers, S. Glöggler, K. V. Kovtunov, M. Plaumann, R. Katz-Brull, K. Buckenmaier, A. Jerschow, F. Reineri, T. Theis, R. V. Shchepin, S. Wagner, P. Bhattacharya, N. M. Zacharias, E. Y. Chekmenev, Angew. Chem. Int. Ed. 2018, 57, 11140–11162.

[18] R. W. Adams, J. A. Aguilar, K. D. Atkinson, M. J. Cowley, P. I. P. Elliott, S. B. Duckett, G. G. R. Green, I. G. Khazal, J. López-Serrano, D. C. Williamson, Science 2009, 323, 1708–1711.

[19] F. Reineri, T. Boi, S. Aime, Nat. Commun. 2015, 6, 5858.

[20] T. Hune, S. Mamone, H. Schroeder, A. P. Jagtap, S. Sternkopf, G. Stevanato, S. Korchak, C. Fokken, C. A. Müller, A. B. Schmidt, D. Becker, S. Glöggler, ChemPhysChem 2023, 24, DOI 10.1002/cphc.202200615.

[21] A. Browning, K. MacCulloch, D. Guarin Bedoya, C. Dedesma, B. M. Goodson, M. S. Rosen, E. Y. Chekmenev, Y.-F. Yen, P. TomHon, T. Theis, Facile Hyperpolarization Chemistry for Molecular Imaging and Metabolic Tracking of [1-13C]Pyruvate in Vivo, Chemistry, 2023.

[22] H. de Maissin, P. Groß, O. Mohiuddin, M. Weigt, L. Nagel, M. Herzog, Z. Wang, R. Willing, W. Reichardt, M. Pichotka, L. Heß, T. Reinheckel, H. Jessen, R. Zeiser, M. Bock, D. von Elverfeldt, M. Zaitsev, S. Korchak, S. Glöggler, J.-B. Hövener, E. Chekmenev, F. Schilling, S. Knecht, A. B. Schmidt, In Vivo Metabolic Imaging of [1-13C]Pyruvate-D3 Hyperpolarized By Reversible Exchange With Parahydrogen, Chemistry, 2023.

[23] M. Goldman, H. Jóhannesson, O. Axelsson, M. Karlsson, Magn. Reson. Imaging 2005, 23, 153–157.

[24] A. B. Schmidt, H. de Maissin, I. Adelabu, S. Nantogma, J. Ettedgui, P. TomHon, B. M. Goodson, T. Theis, E. Y. Chekmenev, ACS Sens. 2022, 7, 3430–3439.

[25] A. Marshall, A. Salhov, M. Gierse, C. Müller, M. Keim, S. Lucas, A. Parker, J. Scheuer, C. Vassiliou, P. Neumann, F. Jelezko, A. Retzker, J. W. Blanchard, I. Schwartz, S. Knecht, J. Phys. Chem. Lett. 2023, 14, 2125–2132.

[26] J. G. Skinner, G. J. Topping, L. Nagel, I. Heid, C. Hundshammer, M. Grashei, F. H. A. Van Heijster, R. Braren, F. Schilling, Magn. Reson. Med. 2023, mrm.29676.

[27] D. K. Hill, M. R. Orton, E. Mariotti, J. K. R. Boult, R. Panek, M. Jafar, H. G. Parkes, Y. Jamin, M. F. Miniotis, N. M. S. Al-Saffar, M. Beloueche-Babari, S. P. Robinson, M. O. Leach, Y.-L. Chung, T. R. Eykyn, PLoS ONE 2013, 8, e71996.

Author Contributions

Data curation: LN, MGi, WG, ZA, AW, MGr, CAM

Funding acquisition: FS, IS

Formal analysis: LN, MGi, WG, ZA, MGr, CAM, GJT, FvH, SK, FS, IS

Investigation: LN, MGi, WG, ZA, MGr, CAM, GJT, FvH, SK, FS

Writing of original draft: LN, MGi, WG, ZA, FS, IS

Discussion of results: all authors

Reviewing and editing of manuscript: all authors